Strain imaging of corroded steel fasteners using neutron transmission imaging

Kanarachos, S., Ramadhan, R. S., Kockelmann, W., Venetsanos, D., Tremsin, A. S. & Fitzpatrick, M. E

DOI 10.1016/j.measurement.2022.111904
ISSN 0263-2241
ESSN 1873-412X

Publisher: Elsevier

Strain imaging of corroded steel fasteners using neutron transmission imaging

Authors: **Stratis Kanarachos[a*], Ranggi S. Ramadhan[b], Winfried Kockelmann[c], Demetrios Venetsanos[d], Anton. S. Tremsin[e], Michael E. Fitzpatrick[a]**

[a]*Faculty of Engineering & Computing, Coventry University, Coventry, CV12JH, UK*
[b]*Institut Laue-Langevin, 71 Avenue des Martyrs, 38000 Grenoble, France*
[c] *STFC, Rutherford Appleton Laboratory, ISIS Facility, Harwell Campus, OX11 0QX, UK*
[d] *Centre for Efficiency and Performance Engineering (CEPE), School of Computing and Engineering, University of Huddersfield, Huddersfield HD1 3DH, UK*
[e] *Space Sciences Laboratory, University of California at Berkeley, CA 94720, USA*

Highlights:

- Quantitative assessment of strain in a bolt/nut assembly using neutron imaging
- Measurements for normal and corroded parts for different bolt preload conditions
- Quantitative analysis of the effect of corrosion on the loss of preloaded tension
- Quantitative analysis of the residual strain on single bolts

Abstract

Various failures in bolted structural connections have caused in the past the collapse of various steel structures exposed to weather conditions, including wind turbine towers, oil and gas platforms, and bridges. Corrosion and the resulting loss of preloaded tension in the bolted connection were the root cause of such catastrophic failures in many cases. However, it is still not fully understood how strain is re-distributed in corroded bolted connections, nor how different factors influence the redistribution. Measuring non-destructively the strain inside the assembly has been the main obstacle. To this end, in this paper, we employed energy-resolved neutron transmission imaging and we present strain maps in corroded bolted connections for the first time. We examined and compared the strain distribution measurements in corroded and non-corroded assemblies for different bolt-tightening techniques. The specimens under investigation were artificially corroded without introducing any additional mechanical loads. The resulting strain maps illustrate how strain is re-distributed and provide insight into the influence of the bolt-tightening method.

Keywords: Bragg-edge analysis, neutron transmission imaging, non-destructive testing, strain distribution, corroded bolt connections

1 Introduction

The structural integrity of high-value critical infrastructure in energy and transportation often depends on the performance of bolted connections. A historical overview of catastrophic incidents showed that bolt malfunctioning is one of the most frequent causes for wind turbine tower collapses [1]. In the investigation following the collapse of wind turbine towers in Taichung Harbor in Taiwan, several bolts had fractured due to the loss of pretension, and signs of corrosion were evident under the bolts' heads [2], [3]. Similar results with regards to the condition of bolted connections were also found in other wind turbine tower collapses [4], [5]. Corroded bolted connections and the loss of preloaded tension also have caused disastrous failures in other structures such as bridges, and equipment in the oil and gas industry [6]. Although original equipment manufacturers prescribe the bolt tightening torque, the resulting clamping force may differ significantly throughout the life of the structure [7].

Different reasons may lead to the loss of pretension in bolted connections; the most frequent ones are excessive rotational vibration, transverse vibration, or axial vibration [7], [8], [9]. Nevertheless, there are also non-vibrational factors that can lead to preloaded tension loss. One of these factors is corrosion, which is common for structures exposed to outdoor weather conditions [10]. To quantify the effect of corrosion on the bolt preload loss Li *et al*. conducted a series of experiments where the bolt head was incrementally milled to emulate corrosion [11]. For an M20 bolt, a 9 mm head-thickness reduction resulted in a clamping force that was approximately half of the initial one. Similar results were obtained when the head bolt diameter of an M20 bolt was reduced by 3 mm. In another set of experiments, Wang *et al*. followed a different approach by artificially corroding bolted joints and comparing the slip load of the bolts before and after corrosion [12]. The experimental results showed a reduction of 50% in the clamping load for a corrosion mass loss of 20%.

To detect bolt looseness different non-destructive methods have been developed [13],[14]. Sah *et al*. estimated the level of bolt tightness by impacting the bolt head in the transverse direction and measuring the first transverse natural frequency [15]. The method distinguished successfully loosened from tightened bolts. Hosoya *et al*. employed a similar method but instead analysed the bending-mode natural frequency of the bolt's threaded portion that protrudes from the nut [16]. Like Sah *et al*. it was possible to distinguish between loosened and tightened bolts. Zhang *et al*. (2018) employed a different technique by introducing a low-frequency pumping vibration that produced a "breathing effect" at the joining interface of the specimens [17]. The nonlinear contact-acoustic response of the bolted joint was exploited to detect loosened and intermediate-tightened joints. Another method for detecting bolt looseness is the electromechanical impedance technique [18]. Piezoelectric transducers (PZT) were glued on the top of the bolts' head. Using the impedance signature and by employing Artificial Neural Networks, Na (2021) distinguished intermediate-tightened from fully tightened joints, with an accuracy ranging between 70% and 95%. In a slightly different setup Qi *et al*. employed two PZTs on the upper plate of one of the specimens and excited the joint using low and high-frequency signals simultaneously [19]. The authors detected successfully the thread loosening phase, which happened at the early stage of bolt joint loosening. Tremsin *et al*. utilised energy-resolved neutron transmission imaging for *in situ* comparisons of strain distributions in fastened joints [20]. Neutron imaging offers the unprecedented advantage of measuring strains in relatively thick samples, and thus can provide a detailed view of the bolt strain map inside fastened assemblies.

Motivated by the previous work described, this study aims to experimentally investigate in greater depth the loss of preloaded tension in bolted connections due to corrosion. To this end, we qualitatively and quantitatively compared the strain distribution of bolted connections, before and after corrosion, using neutron imaging. In addition, we measured the strain distribution for different bolt-tightening techniques and discuss whether this influences preloaded tension loss. The contribution of this paper is summarised as follows:

- We extend the work of Tremsin *et al*. by employing the *in-situ* comparison of strain distributions for corroded fasteners using neutron imaging.
- We measure the strain distribution in bolted connections using neutron imaging for different bolt tightening techniques.
- We qualitatively and quantitatively assess the preloaded tension loss prior and after corrosion using strain distribution maps.
- We analyse and discuss the role of bolt-tightening techniques on the loss of preloaded tension due to corrosion.

The rest of the paper is structured as follows. In Section 2, we explain the methods used in the study: a) the materials used; b) the artificial corrosion method applied; c) the neutron imaging method employed; and d) the measurement procedure followed. In Section 3, we present the measurement results of a single bolt as well as of non-corroded and corroded bolted assemblies for different bolt-tightening techniques. Section 4 discusses the results and provides insight into the role of the bolt-tightening method. In Section 5, conclusions are drawn, and the future research direction is given.

2 Methods

2.1 Materials

In this study, we prepared for the experiments two identical assembly sets. We inserted four M6 bolts of grade 12.9, ISO 4762, into female threads on a stainless steel SS304 workpiece containing two pairs of regular threads drilled next to each other, see Figure 1. The austenitic workpiece material was chosen to allow good separation of Bragg-diffracted neutron spectra from the ferritic high-strength-steel bolts. A stainless-steel spacer bar with a through-hole was fastened by these steel bolts to the bottom bar containing the threads. We used standard commercial off-the-shelf drill bits to drill the threads. The distance of holes from the edges and the spacing between the holes followed the Eurocode EN 1993-1-8:2005.

Each of the four bolts B1-B4 (see Figure 1 left side) was inserted into the workpiece with a different tightening torque (see Table 1):

- Bolt B1: Just inserted into the workpiece until the head of the bolt touched the spacer bar.
- Bolt B2: Tightened with a target torque of 14.5 Nm following ISO 898/1 for unknown coefficient of friction.
- Bolt B3: Tightened with a target torque of 17.4 Nm (20% higher than 14.5 Nm).
- Bolt B4: Tightened with a target torque of 14.5 Nm following a cyclic procedure. The bolt was loosened and retightened to the target torque four times.

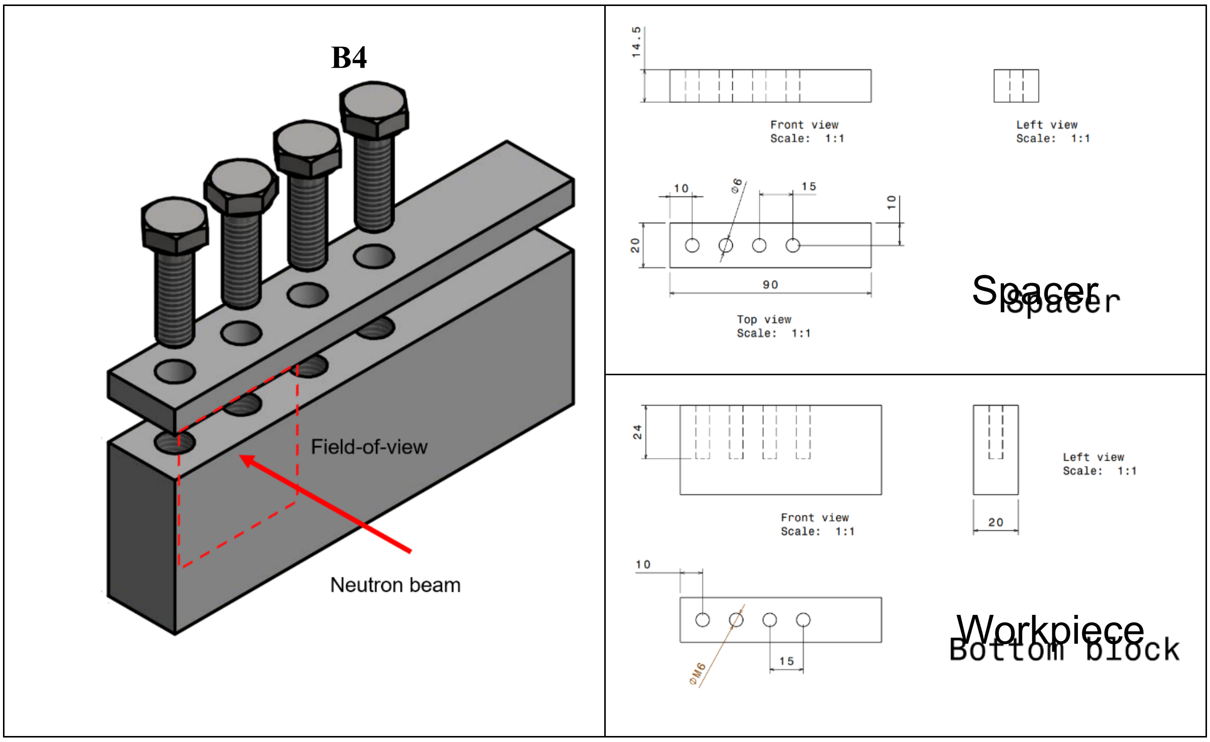

Figure 1 3D view (left) and sketches of the 4-bolt assembly parts (right). Dimensions are in mm

The rationale for using four different tightening techniques is the following. Bolt B1 was inserted without any preload, so the strain distribution for this bolt will be used as the reference state of the unloaded case. For bolt B2 the tightening torque value is the maximum recommended by ISO 898/1 when the coefficient of friction is unknown. For B2, literature informs that the threads nearer to the joint interface carry most of the preload: in particular, the first thread takes approximately three times, while the second one takes almost two times the load the third one does [21]. Due to the unknown, in many cases, coefficient of friction the resulting preload is uncertain and may lead to a greater scatter in practice [9]. For bolt B3 the tightening torque value is 20% higher than bolt B2. The 20% increase guarantees statistically that bolt B3 has a greater preload than B2 [9]. The target torque of 17.4 Nm is lower than the overall maximum allowable tightening torque according to ISO 898/1. Bolt B4 was tightened for a target torque value of 14.5 Nm (same as bolt B2) and then loosened; this cyclic procedure was applied four times. Based on Eccles *et al.*, when a bolt is tightened and then loosened, the preload stabilises to a converged value after the fourth cycle [22]. The preload stabilises due to plastic deformation and relaxation of the first threads and results in a more uniform load distribution between the bolt's threads. Thus, compared to bolt B2 the resulting preload value is much more certain in the case of B4.

Table 1. Details of the bolt fastening procedures

Sample name	Condition
Fastener B1	Inserted without any load until the bolt head touches the spacer (without any preload)
Fastener B2	Tightened to 14.5 Nm

Fastener B3	Tightened to 17.4 Nm
Fastener B4	Tightened to14.5 Nm and loosened 4 times. Finally tightened to 14.5 Nm

Subsequently, one of the two assembly sets was artificially corroded. Following Wang *et al.* the assembly was first placed in a plastic container filled with 5.0% by weight NaCl solution, and then connected to the positive end of an external power supply, see Figure 2(a) [14]. The negative end of the power supply was attached to a copper plate which was also immersed in the solution. A constant electrical current of approximately 300 mA was applied. A picture of the corroded sample is shown in Figure 2(b). The colour of the solution is dark yellow because of the corrosion products. The bolts of the corroded sample are labelled C1 – C4.

a)

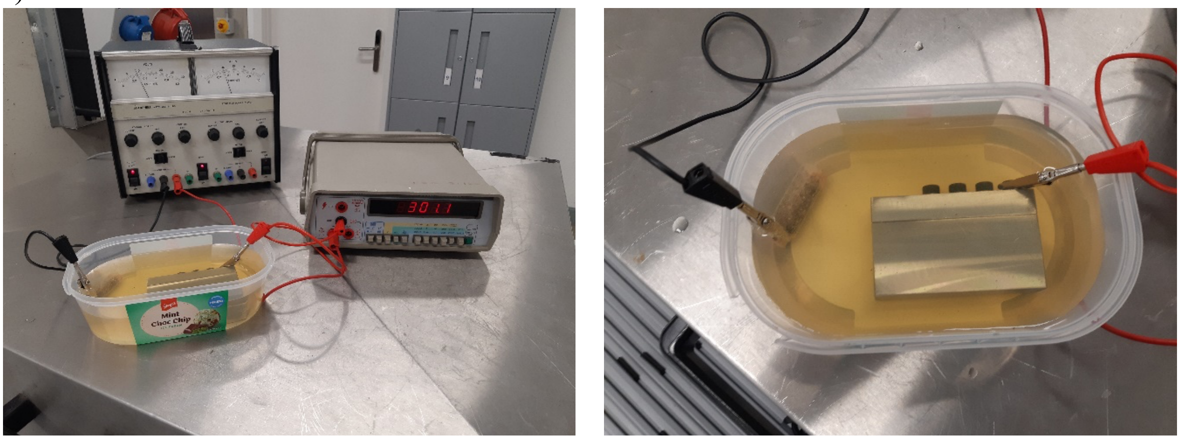

b)

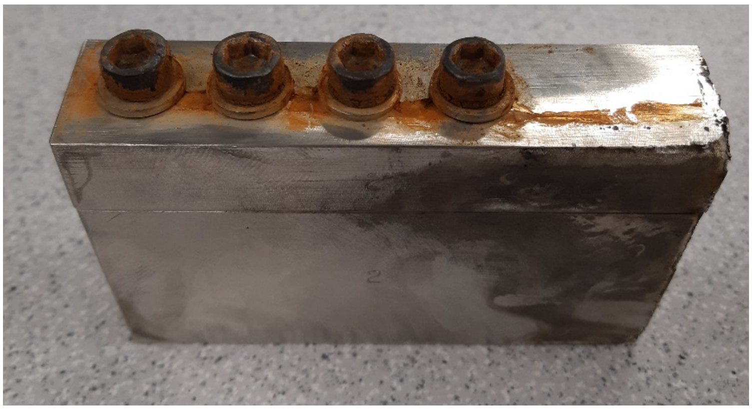

Figure 2 (a) Accelerated corrosion test setup (upper part); and (b) Assembly set after corrosion test (lower part)

The time to target corrosion of the assembly is calculated based on Faraday's law, Eq. 1,

$$t = \frac{m_0 \cdot \eta \cdot z \cdot F}{M \cdot I} \qquad (1)$$

where t is time measured in s, m_0 is the original mass of steel connection measured in g, η is the corrosion induced mass loss, z is the ionic charge (2 for iron), F is a constant (96,500 A·s/mol), M is the atomic weight of the metal (56 g/mol for iron) and I is the corrosion current measured in A. The weighed mass before and after corrosion is 7.7495 g (B1) and 6.9715 g

(C1), respectively, corresponding to a mass loss η of 0.9. This agrees well with the corrosion test duration which was approximately 24 hours long.

2.2 Bragg-edge neutron imaging method

A Bragg-edge neutron transmission spectrum is characterised by a sequence of sudden jumps as a function of neutron wavelength λ. Bragg edges occur at critical wavelengths $\lambda_{hkl} = 2d_{hkl}$ due to coherent backscattering (where the Bragg angle $\theta = 90°$) of neutrons by a family of (hkl) crystal planes that are oriented perpendicular to the beam. Therefore, the wavelength position of a Bragg edge informs about the lattice spacing d_{hkl} which is an interplanar distance of the material, which shrinks or stretches depending on the presence of internal and/or external forces. Using a suitable stress-free reference $d_{0,hkl}$, this lattice spacing can be converted into strain ε, Eq. 2, where λ_{hkl} is Bragg edge position, and d_{hkl} is the lattice spacing:

$$\varepsilon = \frac{\lambda_{hkl} - \lambda_{0,hkl}}{\lambda_{0,hkl}} = \frac{d_{hkl} - d_{0,hkl}}{d_{0,hkl}} \tag{2}$$

The strain is dimensionless and commonly expressed as micro (10^{-6}) strain ($\mu\varepsilon$). For Bragg-edge neutron imaging the camera is placed in the incident beam path, see Figure (a), with the distance between sample and detector *l* as small as possible to minimise blurring due to a finite divergence of the incoming neutron beam. Using this setup, the information of strain in real space is preserved, thus allowing radiographic (2D) strain mapping across the sample. The spatial resolution of the strain map is determined by multiple factors, including pixel size of the detector, beam divergence, and the number of neutrons detected per each pixel [23]. In case the measured transmission spectra in a single pixel is too noisy for the analysis some pixel-binning is implemented. As for other diffraction-based strain measurement techniques, Bragg-edge strain mapping is phase sensitive. This is especially advantageous for the current application, as the transmission spectrum in each detector pixel includes two separated sets of Bragg edges from the bolt and workpiece, respectively. The strains from the two components can be independently analysed as long as the Bragg edges are well-separated. This allows the *in-situ* investigation of preloaded bolts.

2.3 Measurement details and data analysis

Energy-resolved neutron radiograms were collected on the IMAT beamline [24, 25] at the ISIS pulsed neutron source. A detailed study on the performance and capability of IMAT can be found in [23]. The experimental parameters are summarized in Table 2, and the setup is shown in Figure . The instrument uses a ‘pinhole setup’, using a circular neutron collimator of 60 mm diameter about *L*~10.5 m upstream of the transmission detector. This geometry defines a quasi-parallel neutron beam, with a divergence given by an *L*/*D* of about 175. 'A microchannel plate (MCP)/Timepix pixel detector [26] at 56.5 m and the pinhole collimator at 10.5 m from the neutron source, respectively, was synchronized to the 10 Hz pulsed neutron source. The MCP detector consisted of a stack of MCPs, with a neutron-sensitive MCP on the beam-facing side, in front of a 2 × 2 array of Timepix charge readout chips with 256 × 256 pixels each, and 55 × 55 μm^2 pixels resulting in a field of view (FoV) of 28 × 28 mm^2. For each registered neutron the MCP detector measured its time-of-flight (ToF), from which the wavelength that specific neutron was derived [25]. Accumulation of many neutrons per pixel resulted in the measurement of neutron transmission spectra in each pixel of our dataset, integrated through the sample thickness along the direction of the neutron beam.

The low-indexed Bragg edges of the two steel phases were recorded by using the IMAT neutron wavelength range from 0.7 to 5 Å, corresponding to a ToF range of 10 - 70 ms. This setting enabled the observation of the first Bragg edges of ferrite (110 at 4.055 Å) and austenite (111 at 4.145 Å), Figure 4. The ToF range between two successive ISIS pulses (1/10Hz = 100 ms) was subdivided into four acquisition frames per neutron pulse (Table 2); in other words, the MCP detector was read-out four times between neutron pulses, to reduce dead-time effects due to event-overlaps [27]. For each acquisition, a stack of 2345 ToF radiograms was obtained corresponding to a narrow ToF bin of 20 μs and 40 μs below and above a neutron wavelength of 4.5 Å, respectively. The flight path (56.53 m) from the neutron source to the MCP detector was calibrated using data collected on a 10-mm ferritic Fe rod with a well calibrated d_0 value.

The fastener samples were mounted on an aluminium frame just in front the MCP detector, see Figure (b). Given the MCP sensor size of 28 × 28 mm^2, eight separate radiography stacks were collected, each capturing two bolts (upper or lower parts) at a time. Data for a separate bolt, mounted in air, was collected for comparison. For collection of an open-beam radiogram stack, the sample was moved out of sight of the MCP. The distance from the bolt centre to the neutron sensitive MCP was 32 mm; hence the geometric blur of 32/173=0.185 mm. The direction of the neutron beam and, hence the measured strain component, is indicated in Figure (a).

Table 2. Neutron imaging parameters

Parameter	**Value**
Source-to-sample distance / m	56.53
Pinhole-to-sample distance (*L*) / m	10.53
Neutron spectral range / Å	Cold: 0.7 - 5
Incident neutron flux / n/cm^2/s	1.2 . 10^7
Sample-to-camera sensor distance / mm	32
Pinhole diameter (*D*) / mm	60
Collimation ratio (*L*/*D*)	175
Average geometric blur / mm	0.185
Camera type	MCP with a quad Timepix readout Time resolving; 512 × 512 pixels
ToF settings: from, to / ms	10 – 24.7 / 25-37.7 / 38-47.7 / 48 -65
ToF channel width / ms	0.02 and 0.04
Number of ToF slices / radiographies per stack	2345
Pixel size / mm^2	0.055 × 0.055
Effective pixel size / mm^2	~0.65 × 0.65
Exposure time / hours	4 per one dataset (stack of images)

The radiographic stacks were corrected for event overlaps [27], and flat-fielded in the region of analysed Bragg edges by using a wavelength-averaged radiography and a pixel-averaged open-beam spectrum, generated from the open-beam stack. Figure 4a displays examples of Bragg-edge transmission curves for one of the bolts and the workpiece. For the maps shown, the strongest Bragg edges were selected: {110} for the ferritic phase, and {111} for the austenitic phase. These lattice planes are considered to have low sensitivity to intergranular strains for the corresponding materials, and thus better represent the bulk behaviour of the materials under stress [Neutron ISO standard]. Bragg edge positions, λ_{hkl}, were fitted using an analytical function, as described in Eq. 3 [28]. Widths of Bragg edges, related to parameters σ and τ in Eq. 3, were determined using a large region of interest for one of the bolts (B1), and then kept fixed for the strain mapping for all bolts. To improve the accuracy of fitting by increasing the number of counts in measured transmission spectra, 20 × 20 MCP pixels were combined into a macro-pixel, and a running average with a step size of 55 μm was implemented. The effective spatial resolution is determined from the combination of geometric blur and macropixel size, which relation is given in [23]; in this case the value is ~0.65 mm. Three parameters were fitted for each Bragg edge and each macro-pixel: the Bragg edge baseline C_1, Bragg edge height C_2, and position λ_{hkl}.

$$T(\lambda) = C_1 + C_2 \left[\operatorname{erfc}\left(\frac{\lambda_{hkl}-\lambda}{\sqrt{2}\sigma}\right) - \exp\left(\frac{\lambda_{hkl}-\lambda}{\tau} + \frac{\sigma^2}{2\tau^2}\right) \times \operatorname{erfc}\left(\frac{\lambda_{hkl}-\lambda}{\sqrt{2}\sigma} + \frac{\sigma}{\sqrt{2}\tau}\right)\right] \quad (3)$$

Figure 4(b) illustrates the fitting process for a double-Bragg edge, yielding Bragg edge positions of the $\lambda_{110} = 4.055$ Å of the ferritic phase of the bolt, and $\lambda_{111} = 4.145$ Å of the austenitic phase of the workpiece.

The fitted Bragg edge positions were converted into strains using Eq. 2, using d_0 values of $d_0 = 4.054$ Å for the ferritic phase, and $d_0 = 4.148$ Å for the austenitic phase. The d_0 values were determined by averaging Bragg-edge positions from regions where the stresses are assumed to be minimum, *i.e.*, at the bottom end of the bolt and at the bottom part of the workpiece. The Bragg edge positions from these areas have been determined to an accuracy of 2.5E-4 Å or equivalent precision of around 65 με. It is important to note, however, that the main point of d_0 value here is not to provide the absolute strain values, but rather to provide a baseline value to compare the relative strain level in the bolts with different preloads and level of corrosion. Propagating the error of the fitted Bragg edge position, using 20 × 20 MCP pixels used in this paper, to the calculated strain, the strain error is calculated to be approximately 180-260 microns.

Four 28 × 28 mm^2 maps of each assembly, the uncorroded and corroded one, were stitched together for thresholding and presentation purposes. A thresholding algorithm in the image processing software ImageJ was used for quantifying the strained regions in the bolt and workpiece, respectively. The threshold was determined based on the min-max strains measured on the uncorroded single bolt, see Figure 6, as this represents the unloaded cases.

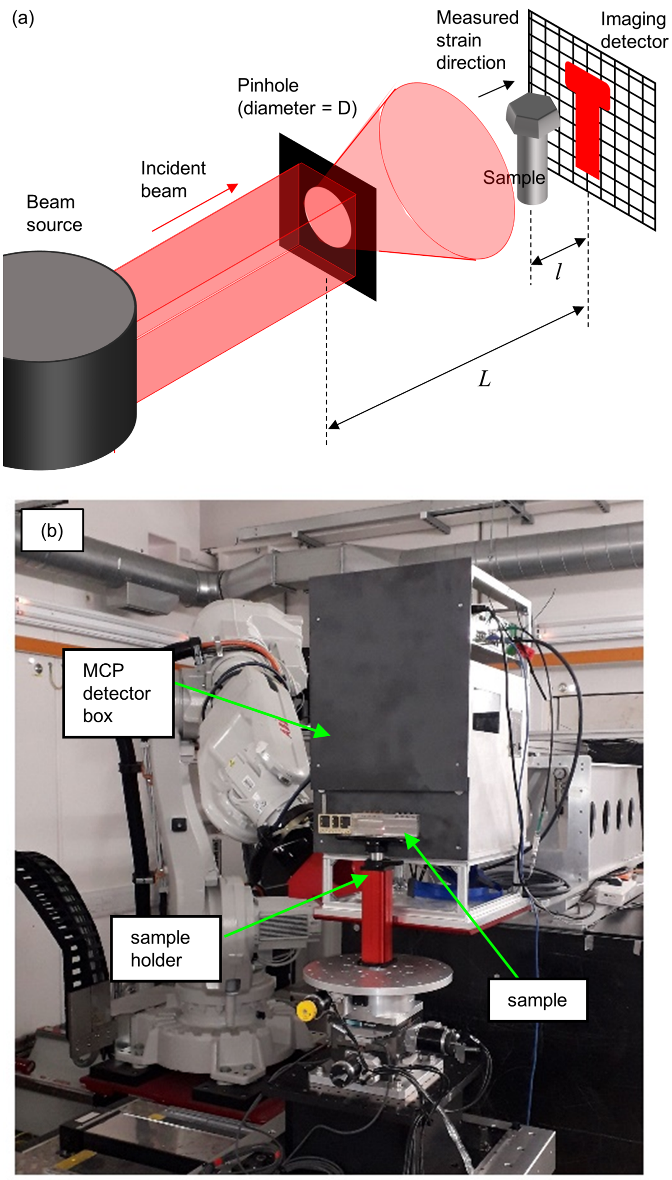

Figure 3 (a) Schematic of the neutron imaging setup, indicating the measured strain direction which is parallel to the beam direction, the pinhole collimator (diameter D = 60 mm) at a distance L~10.5 m from the detector, and a sample-to-detector distance l = 32 mm. Note that the schematic exaggerates the conical expansion of the neutron beam from the pinhole; (b) Photo of the sample setup in front of the MCP camera box on IMAT.

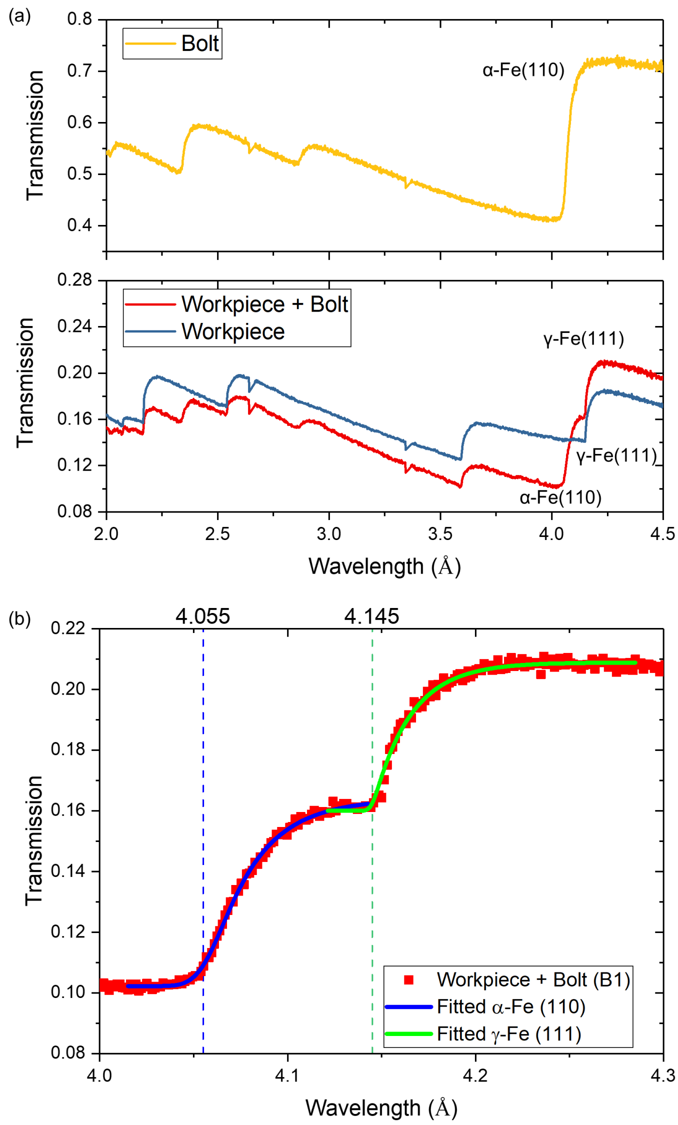

Figure 4 (a) Transmission spectra of one of the bolts (yellow line), workpiece (blue line), and the convolution of the two (red line); (b) Examples of the fitting of Bragg edges using Eq. 3 for the α-Fe(110) (blue line) and γ-Fe(111) (green line). Note that a Bragg-edge position is located at the foot of a Bragg-edge due to the asymmetry of the time-of-flight pulse shape of the neutron source.

3 Results

Figure shows the radiographs of the uncorroded (bolts B1-B4) and corroded (bolts C1-C4) bolt assemblies. The radiographs are integrated over the whole wavelength range of the beam, therefore they are equivalent to the radiographs taken on continuous-source beamlines. The radiographs are presented for the same contrast settings for comparison. The lighter regions indicate higher neutron transmission for empty holes. The darker areas at the bottom part of the tapped holes indicate low neutron transmission due to metal chips from the hole drilling. The color changes at the interface of the bolt to air boundary. The white area – that is where there was no bolt, leading to less attenuation in that area, only threaded hole in the base plate. The darker areas within the bolt thread in the corroded images are due to the small amount of liquid which was not fully dried out from the tight space between the bolt and the threaded hole. Generally, white grey values signify high transmission. White grey values in the workpiece section indicate low attenuation, especially where the bolt stops reaching into the thread. The transmission, given by Beer Lambert's law, is high were the product of through-thickness and attenuation coefficient is high. We assume that the amount of tapping fluid was similar for both work pieces (uncorroded and corroded), and we assume that the higher number of dark spots and dark areas in Figure 5 in the corroded work piece originates from residual moisture from the exposure to the electrolyte (Figure 2a).

From the radiographs it can be observed that the corroded bolt heads are noticeably smaller compared to the non-corroded ones. A quantitative comparison between the non-corroded bolts (B1-B4) and the corroded ones (C1-C4) shows on average a 10% reduction in the number of grey pixels at the bolts' head.

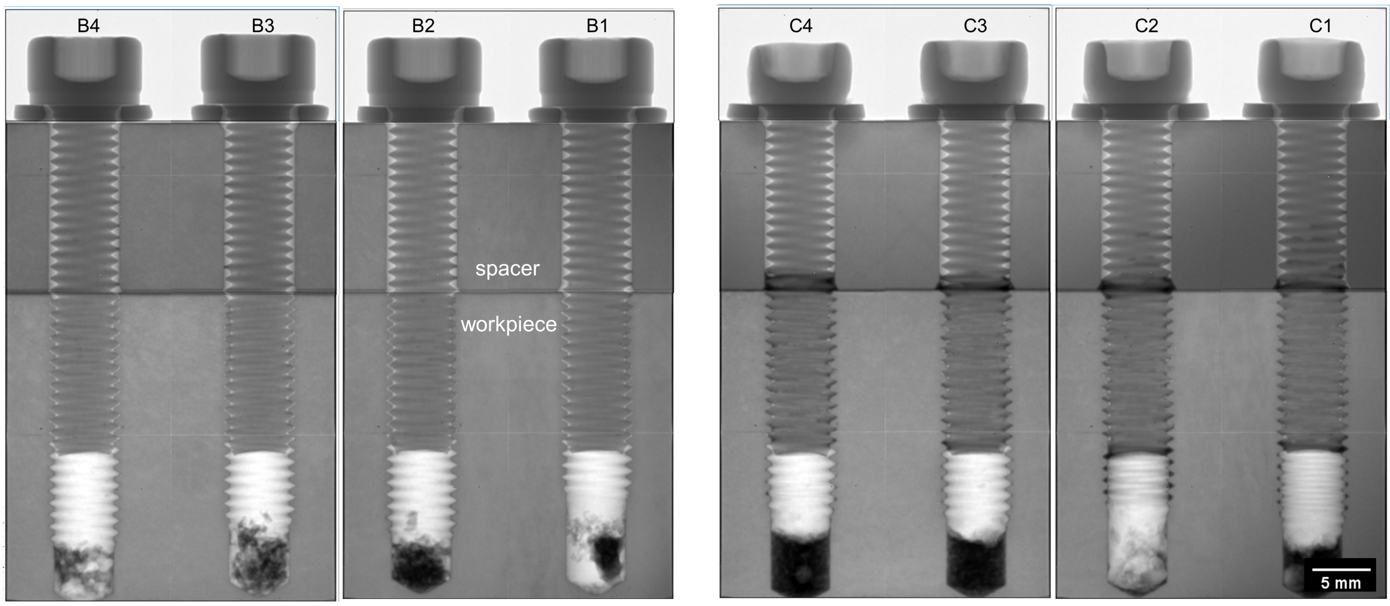

Figure 5 Radiographs of the non-corroded (B1-B4) and corroded (C1-C4) bolt assemblies.

Figure (a) shows the radiograph of a bolt measured in air, separate from the workpiece, to assess the influence of the workpiece on the analysis of the bolt and to aid selection of thresholding levels. A strain map was reconstructed from the measurement and is shown in Figure (b). A suitable colour scale was chosen to mask any pre-existing residual strains in the bolts and to highlight the strains applied during the bolt preloading. This is done by firstly reconstructing the strain map for the bolt measured in air, i.e., no external loading, and any strain variations in the bolt are due to the residual stresses and/or noise in the data. Color scale shown in Figure 6 (b) was then applied, where threshold values were set. Most of the initial strain variation fell between a certain threshold range, therefore showing a single color. This means the initial strain variations are masked and, assuming the residual strain level for all bolts are similar, the strain map in Figure 6(b) can be used as the baseline of unloaded state of the bolts. Any strain values beyond the corresponding threshold range will appear as different color, as shown in Figure 7(a) and (b), indicating the strains induced by the preload.

Using the selected colour scale, the strain map showed that the bolt body strains outside the workpiece are within a range 0 to –2000 με. The same colour scale was applied to the strain maps of the non-corroded and corroded bolt assemblies, and the results are shown in Figure . It is noted that slightly elevated strain levels at the bottom of the bolt heads indicate a limitation of the strain analysis method, i.e. that strain components are averaged along the neutron path and that strain readings can appear similar for differently manufactured parts such as the heads compared to the threads.

Inspection of Figure (a) shows that bolt B1, which was inserted without any preload, has tensile strains in the range of 250-1500 με (amber colour) shown by the appearance of the amber area. The appearance of tensile strain is more pronounced in bolt B2 (preloaded with nominal torque) and even more in bolt B3 (20% more torque was applied than B2) where strain values up to 3200 με (red color) were observed. Meanwhile, the tensile strain in bolt B4 (nominal torque followed by loosening and retightening) is less pronounced compared to B3 and comparable but higher to B2. Figure (b) indicates that for the same preload conditions, the tensile strains inside the corroded bolts are significantly lower. Elevated tensile strains in the upper part of the unloaded C1 specimen in the spacer regions are visible. On the other hand, as shown in Figure 8, the compressive strains in the workpiece and spacer around the upper part of bolt C1 are not elevated. Therefore, it is not yet understood why the strains in the upper part of the unloaded C1 specimen are elevated as this also not expected from a theoretical point of view.

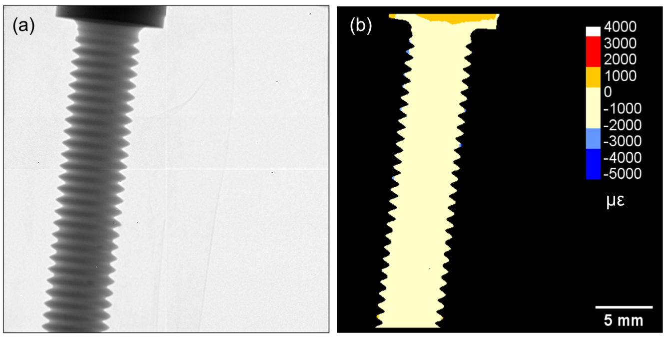

Figure 6 (a) Radiograph and (b) strain map of a bolt outside the assembly.

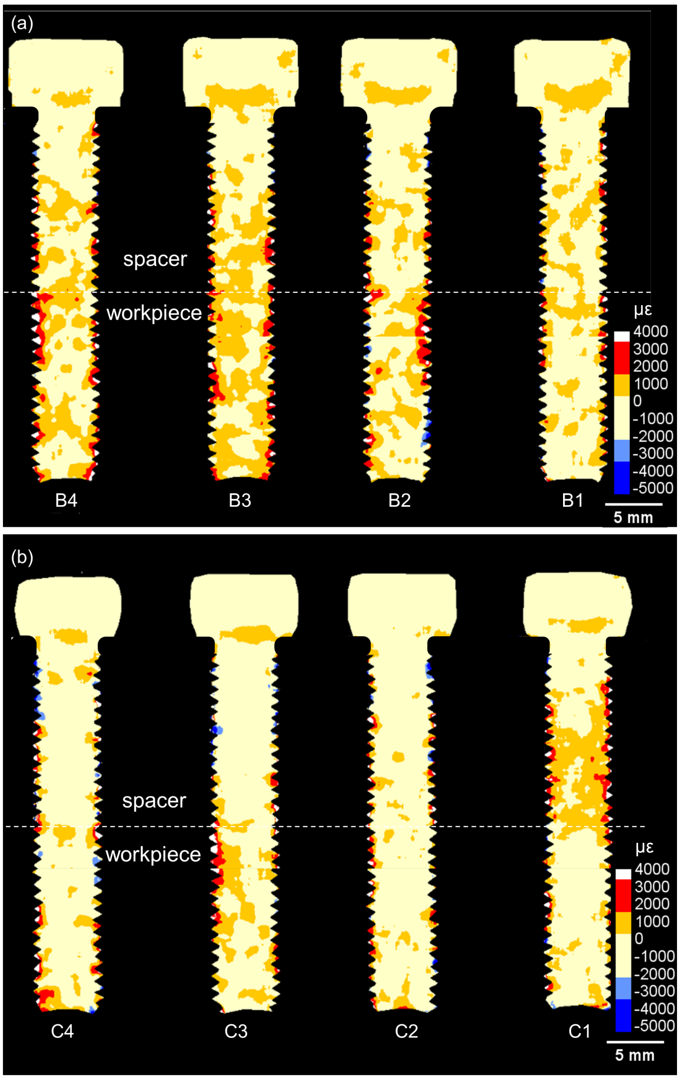

Figure 7 Strain maps of (a) non-corroded and (b) corroded bolts inside the assembly. Amber and red colours indicate tensile strains between 250 – 1500 με and 1500 – 3200 με, respectively.

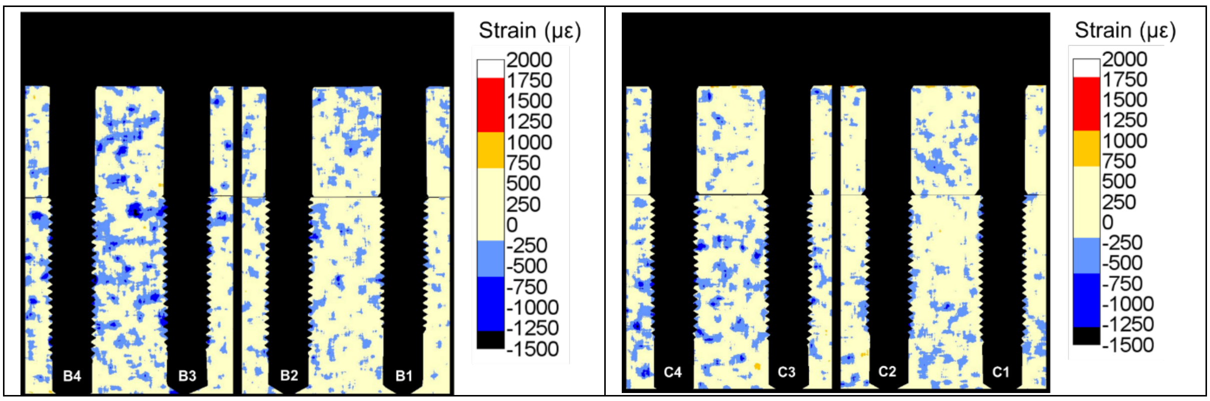

Figure 8 Strain maps of the workpiece and spacer for the (a) non-corroded and (b) corroded bolts inside the assembly. Blue colours indicate tensile strains between -250 and -1500 με.

To provide a quantitative comparison to the visual observation, a statistical image analysis was performed by counting the percentages of the tensile strain area, as a number of pixels, in the lower parts of the bolts. The results are illustrated in Figure . The unloaded B1 and C1 specimens show almost identical percentages of tensile strain areas of around 10%. Preloading the bolt with a nominal torque (B2) increased the percentage to approximately 26%. After corrosion, the percentage drops to around 9% (C2). The highest percentage of tensile strain was observed on the overtightened bolt (B3), with a value of about 39%. The corrosion process on the similarly overtightened bolt (C3) reduced the percentage to 19.5%. For the bolts which were tightened to nominal torque and then loosened and re-tightened, the percentages were 31% and 14.5% for the uncorroded (B4) and corroded (C4) bolts, respectively.

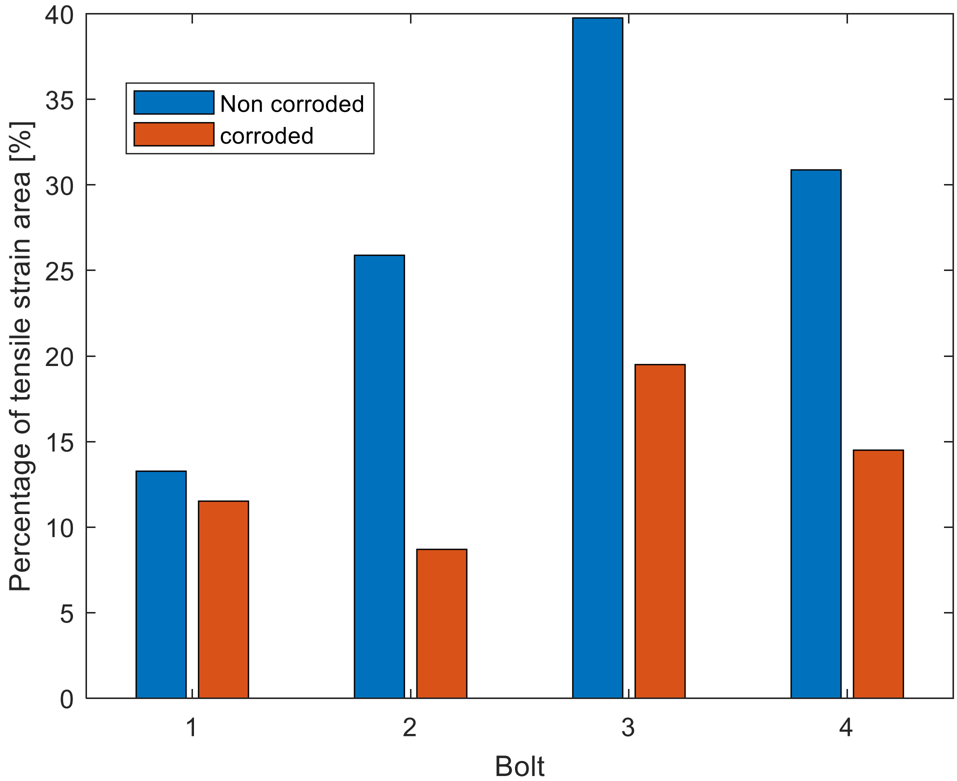

Figure 9 Comparison of the percentage of tensile strain area between non-corroded and corroded bolts.

4 Discussion

There are certain aspects that need to be discussed regarding the strain measurement on the fastener assembly using Bragg-edge imaging. Firstly, as mentioned earlier and shown in Figure (a), the measured strain direction is parallel with the beam propagation direction. Therefore, the strains displayed in Figure and Figure (a) and Figure 7(b) are convolutions of shear and axial strains. Secondly, the imaging results are 2D projections of the bolt. Since the bolts have a generally cylindrical geometry, the neutrons traverse more material towards the centre of the bolt projection and less material towards the edge of the projection. Consequently, the Bragg-edge signal is statistically better towards the centre of the specimen, *i.e.*, the precision of the strain determination is lower in the thread region. Therefore, one should be mindful in interpreting the strain results towards the edge of the specimen, especially on the threads of the bolt. Lastly, the relative strain values need to be interpreted within the context of the d_0-reference approach that was used in this study.

Within these limitations, Bragg-edge imaging provides a unique capability to measure and compare strains inside bolt specimens which were subjected to different preloads. The degree of tensile strains, mainly observed on the bottom parts of the bolts that were engaged to the workpiece, correlates with the preload levels and agree with theoretical results from the literature.

In particular, although we inserted bolt B1 without any preload into the workpiece, the subsequent tightening of bolts B2-B4 led to a tighter contact between the spacer and workpiece and thus into small tension in bolt B1. Indeed, we expected only small tension as the distance between the bolts followed the recommendation of Eurocode EN 1993-1-8:2005.

Furthermore, the tightening of the bolts was achieved using a typical torque control method, thus the torque T applied to a bolt is anticipated to cause a linearly proportional bolt pretension F [29]. Since the applied torques were $T3 > T2 > T1$ for the bolts B3, B2 and B1, respectively, it is anticipated that $F3 > F2 > F1$. Furthermore, the repeated tightening applied to the bolt B4 is anticipated to result in a pretension slightly higher than that achieved with the first tightening, thus $F4 > F2$, because lubricant for bolt tightening was sparingly used [30, 31]. The analysis of the 2D strain maps, obtained with the proposed neutron diffraction approach, showed that a similar qualitative correlation exists between bolt pretension and percentage of the tensile area of the respective strain maps (Figure 8, columns for the uncorroded bolts). The respective quantitative correlation is an objective for further study as the residual strains due to bolt manufacturing need to be taken into account.

The differences between the uncorroded B1–B4 and corroded C1–C4 bolts are mainly due to two factors:

i) The flexible washer, which was put between each bolt head and the spacer, acts as a spring, pushing back against the pressure imposed by the bolt head. Over time, and especially within a corrosive environment, the washer may lose its springiness and lead to loss of the clamping force [33].
ii) The reduction of the volume of the bolt head results in the reduction of the respective clamping force [34, 35, 36, 37].

Based on the above reasons, it is theoretically anticipated that corrosion will cause a high loss of pretension, the bolt B1 being an exception, as it was tightened by hand thus had very small (negligible) pretension compared to the other bolts. Furthermore, since the corrosive environment was the same for all bolts, it is also theoretically anticipated that the loss of pretension would be rather uniform across the bolts B2, B3 and B4. The measurements show that bolts C2-C4 have lost more than 50% of the initial preload for a bolt mass loss of 10%. This agrees with the results presented in [13] and [14] when considering the difference in the bolt sizes. More importantly, the measurement of the corroded bolts clearly demonstrates the relaxation of these strains due to the corrosion process. The preload loss due to corrosion was expected and has been mentioned previously in the literature [38, 39].

The difference in the resulting preload shows the importance of the tightening method and target value when corrosion takes place. For the practitioner, a complete map between different corrosion levels and the remaining strain level is required. Such maps can be used for predictive maintenance purposes.

Conclusions

In this study, we experimentally investigated the loss of preloaded tension in bolted connections when corrosion takes place and in the absence of any mechanical loads. To measure the loss of preloaded tension in the fasteners we employed neutron imaging and were able to visualise non-destructively the developed strains inside the assembly before and after corrosion. We explored the influence of the tightening torque level on the loss of bolt preload by using two different target values following ISO898/1. Furthermore, we investigated the impact of a tightening method that leads to a more uniform load distribution between the threads of the bolt.

The conclusions from this work are as follows:

- Neutron imaging successfully mapped the developed strains inside the bolted connections. The numerical results obtained agreed with the ones known from the literature for the non-corroded bolts.
- For the first time, we were able to see the strain developed in corroded fasteners. In the absence of any external mechanical load a loss of bolt mass by 10% led to a complete loss of the preload in two out of three cases investigated. In the third case, the preloaded tension was reduced but not to an insignificant level.

These findings have significant practical value and have consequences for the structural analysis of bolted connections where corrosion may occur or has already occurred. Future work will focus on different material systems and corrosion conditions.

Acknowledgements

The experiment was carried out at the ISIS Neutron and Muon Source of the UK Science and Technology Facilities Council (STFC) https://doi.org/10.5286/ISIS.E.RB1920620. M. E. Fitzpatrick is grateful for funding from the Lloyd's Register Foundation, a charitable foundation helping to protect life and property by supporting engineering-related education, public engagement and the application of research.

The accelerated corrosion experiment was carried out by Mr James Jarvis, Faculty of Engineering, Environment and Computing, Coventry University, UK.

Reference

1. Ma, Y., Martinez-Vazquez, P., & Baniotopoulos, C. (2019). Wind turbine tower collapse cases: a historical overview. Proceedings of the Institution of Civil Engineers - Structures And Buildings, 172(8), 547-555. doi: 10.1680/jstbu.17.00167
2. Chou, J., & Tu, W. (2011). Failure analysis and risk management of a collapsed large wind turbine tower. Engineering Failure Analysis, 18(1), 295-313. doi: 10.1016/j.engfailanal.2010.09.008
3. Chou, J., Ou, Y., & Lin, K. (2019). Collapse mechanism and risk management of wind turbine tower in strong wind. Journal Of Wind Engineering And Industrial Aerodynamics, 193, 103962. doi: 10.1016/j.jweia.2019.103962
4. Bolts blamed for V112 collapse. (2021). Retrieved 2 October 2021, from https://renews.biz/38563/bolts-blamed-for-v112-collapse/
5. Fatigue Failure Accident of Wind Turbine Tower in Taikoyama Wind Farm (2021). Retrieved 2 October 2021, from http://windeng.t.u-tokyo.ac.jp/ishihara/proceedings/2015-9_ppt.pdf
6. Zhou, M., Yang, D., Hassanein, M., Zhang, J. and An, L., (2017). Failure analysis of high-strength bolts in steel truss bridges. Proceedings of the Institution of Civil Engineers - Civil Engineering, 170(4), pp.175-179.
7. Liu, J., Ouyang, H., Peng, J., Zhang, C., Zhou, P., Ma, L., & Zhu, M. (2016). Experimental and numerical studies of bolted joints subjected to axial excitation. *Wear*, *346-347*, 66-77. https://doi.org/10.1016/j.wear.2015.10.012
8. Li, Z., Chen, Y., Sun, W., Jiang, P., Pan, J., & Guan, Z. (2021). Study on self-loosening mechanism of bolted joint under rotational vibration. Tribology International, 161, 107074. https://doi.org/10.1016/j.triboint.2021.107074
9. Zhang, M., Zeng, D., Lu, L., Zhang, Y., Wang, J., & Xu, J. (2019). Finite element modelling and experimental validation of bolt loosening due to thread wear under transverse cyclic loading. Engineering Failure Analysis, 104, 341-353. https://doi.org/10.1016/j.engfailanal.2019.05.001
10. Bickford, J. (2008). *Introduction to the design and behavior of bolted joints*. CRC Press.
11. Li, M., Yao, L., Zhang, S., Wang, D., He, Z., & Sun, G. (2021). Study on bolt head corrosion influence on the clamping force loss of high strength bolt. *Engineering Failure Analysis*, *129*, 105660. doi: 10.1016/j.engfailanal.2021.105660
12. Wang, H., Tang, F., Qin, S., Tu, K., & Guo, J. (2020). Corrosion-Induced Mechanical Degradation of High-Strength Bolted Steel Connection. *Journal Of Materials In Civil Engineering*, *32*(8), 04020203. https://doi.org/10.1061/(asce)mt.1943-5533.0003275
13. Wang, L., Yuan, B., Xu, Z., & Sun, Q. (2022). Synchronous detection of bolts looseness position and degree based on fusing electro-mechanical impedance. Mechanical Systems And Signal Processing, 174, 109068. doi: 10.1016/j.ymssp.2022.109068
14. Jiang, J., Chen, Y., Dai, J., & Liang, Y. (2022). Multi-bolt looseness state monitoring using the recursive analytic based active sensing technique. Measurement, 191, 110779. doi: 10.1016/j.measurement.2022.110779
15. Sah, S., Thomsen, J., Brøns, M., Fidlin, A., & Tcherniak, D. (2018). Estimating bolt tightness using transverse natural frequencies. *Journal Of Sound And Vibration*, *431*, 137-149. https://doi.org/10.1016/j.jsv.2018.05.040
16. Hosoya, N., Niikura, T., Hashimura, S., Kajiwara, I., & Giorgio-Serchi, F. (2020). Axial force measurement of the bolt/nut assemblies based on the bending mode shape frequency of the protruding thread part using ultrasonic modal analysis. *Measurement*, *162*, 107914. https://doi.org/10.1016/j.measurement.2020.107914

17. Zhang, Z., Liu, M., Liao, Y., Su, Z., & Xiao, Y. (2018). Contact acoustic nonlinearity (CAN)-based continuous monitoring of bolt loosening: Hybrid use of high-order harmonics and spectral sidebands. *Mechanical Systems And Signal Processing*, *103*, 280-294. https://doi.org/10.1016/j.ymssp.2017.10.009
18. Na, W. (2021). Bolt loosening detection using impedance based non-destructive method and probabilistic neural network technique with minimal training data. *Engineering Structures*, *226*, 111228. https://doi.org/10.1016/j.engstruct.2020.111228
19. Qin, X., Peng, C., Zhao, G., Ju, Z., Lv, S., & Jiang, M. et al. (2021). Full life-cycle monitoring and earlier warning for bolt joint loosening using modified vibro-acoustic modulation. *Mechanical Systems And Signal Processing*, *162*, 108054. https://doi.org/10.1016/j.ymssp.2021.108054
20. Tremsin, A., Yau, T., & Kockelmann, W. (2016). Non-destructive Examination of Loads in Regular and Self-locking Spiralock® Threads through Energy-resolved Neutron Imaging. *Strain*, *52*(6), 548-558. https://doi.org/10.1111/str.12201
21. Lu, S., Hua, D., Li, Y., Cui, F., & Li, P. (2019). Load and Stress Distribution of Thread Pair and Analysis of Influence Factors. Journal Of Physics: Conference Series, 1187(3), 032060. https://doi.org/10.1088/1742-6596/1187/3/032060
22. Eccles, W., Sherrington, I., & Arnell, R. (2010). Frictional changes during repeated tightening of zinc plated threaded fasteners. Tribology International, 43(4), 700-707. https://doi.org/10.1016/j.triboint.2009.10.010
23. Ramadhan, R., Kockelmann, W., Minniti, T., Chen, B., Parfitt, D., Fitzpatrick, M., & Tremsin, A. (2019). Characterization and application of Bragg-edge transmission imaging for strain measurement and crystallographic analysis on the IMAT beamline. *Journal Of Applied Crystallography*, *52*(2), 351-368. https://doi.org/10.1107/s1600576719001730
24. Minniti, T., Watanabe, K., Burca, G., Pooley, D., & Kockelmann, W. (2018). Characterization of the new neutron imaging and materials science facility IMAT. *Nuclear Instruments And Methods In Physics Research Section A: Accelerators, Spectrometers, Detectors And Associated Equipment*, *888*, 184-195. https://doi.org/10.1016/j.nima.2018.01.037
25. Kockelmann, W., Minniti, T., Pooley, D., Burca, G., Ramadhan, R., & Akeroyd, F. et al. (2018). Time-of-Flight Neutron Imaging on IMAT@ISIS: A New User Facility for Materials Science. *Journal Of Imaging*, *4*(3), 47. https://doi.org/10.3390/jimaging4030047
26. Tremsin, A., Vallerga, J., McPhate, J., & Siegmund, O. (2015). Optimization of high count rate event counting detector with Microchannel Plates and quad Timepix readout. Nuclear Instruments And Methods In Physics Research Section A: Accelerators, Spectrometers, Detectors And Associated Equipment, 787, 20-25. https://doi.org/10.1016/j.nima.2014.10.047
27. Tremsin, A., Vallerga, J., McPhate, J., & Siegmund, O. (2014). Optimization of Timepix count rate capabilities for the applications with a periodic input signal. Journal Of Instrumentation, 9(05), C05026-C05026. https://doi.org/10.1088/1748-0221/9/05/c05026
28. Tremsin, A., McPhate, J., Kockelmann, W., Vallerga, J., Siegmund, O., & Feller, W. (2009). Energy-Resolving Neutron Transmission Radiography at the ISIS Pulsed Spallation Source With a High-Resolution Neutron Counting Detector. IEEE Transactions On Nuclear Science, 56(5), 2931-2937. https://doi.org/10.1109/tns.2009.2029690

29. Budynas, R.G. and Nisbett, K.J., (2010) Shigley's Mechanical Engineering Design (9^{th} ed), McGraw-Hill (ISBN-13: 978-0073529288)
30. Zheng M., Liu Z., Yan X., Niu N., Zhang T., Li Y.(2022) Initial losing behavior of pre-tightening force for threaded fastener during repeated tightening; Engineering Failure Analysis, https://doi.org/10.1016/j.engfailanal.2021.106021)

31. Liu Z., Zheng M., Yan X., Zhao Y., Cheng Q., Yang C.(2020) Changing behavior of friction coefficient for high strength bolts during repeated tightening, Tribol. Int., 10.1016/j.triboint.2020.106486
32. Lee, Y.-L., & Ho, H.-C. (2012). Design and Analysis of Metric Bolted Joints. Metal Fatigue Analysis Handbook, 461–513. doi:10.1016/b978-0-12-385204-5.00012-4).
33. Cui, E., Zuo, C., Fan, M. et al. (2021) Monitoring of corrosion-induced damage to bolted joints using an active sensing method with piezoceramic transducers. J Civil Struct Health Monit 11, 411–420. https://doi.org/10.1007/s13349-020-00457-6)
34. Li, M., Yao, L., Zhang, S., Wang, D., He, Z., & Sun, G. (2021). Study on bolt head corrosion influence on the clamping force loss of high strength bolt. Engineering Failure Analysis, 129, 105660 (doi: 10.1016/j.engfailanal.2021.105660)
35. Ahn J-H, Lee JM, Cheung J-H, Kim I-T (2016) Clamping force loss of high-strength bolts as a result of bolt head corrosion damage: experimental research A. Eng Fail Anal 59:509–525 (doi.org/10.1016/j.engfailanal.2015.08.037)
36. Chao Jiang, Wen Xiong, C.S. Cai, Yichen Zhu, Jia Wang (2022) Preload loss of high-strength bolts in friction connections considering corrosion damage and fatigue loading (doi.org/10.1016/j.engfailanal.2022.106416)
37. Wang, H., Tang, F., Qin, S., Tu, K., & Guo, J. (2020). Corrosion-Induced Mechanical Degradation of High-Strength Bolted Steel Connection. Journal of Materials in Civil Engineering, 32(8), 04020203. doi:10.1061/(asce)mt.1943-5533.0003275
38. Lachowicz, M., & Lachowicz, M. (2021). Influence of Corrosion on Fatigue of the Fastening Bolts. Materials, 14(6), 1485. https://doi.org/10.3390/ma14061485
39. Hui-li, W., & Si-feng, Q. (2014). High-Strength Bolt Corrosion Fatigue Life Model and Application. The Scientific World Journal, 2014, 1-5. https://doi.org/10.1155/2014/